Ecological Informatics 87 (2025) 103099

Contents lists available at ScienceDirect

Ecological Informatics

journal homepage: www.elsevier.com/locate/ecolinf

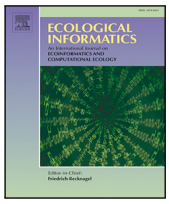

Coral reef detection using ICESat-2 and machine learning

Gabrielle A. Trudeau [a,b,*], Kim Lowell [a], Jennifer A. Dijkstra [a]

[a] Center for Coastal and Ocean Mapping/UNH-NOAA Joint Hydrographic Center, University of New Hampshire, Durham, NH 03824, USA
[b] Integrated Applied Mathematics Program, Department of Mathematics and Statistics, University of New Hampshire, Durham, NH 03824, USA

ARTICLE INFO

Dataset link: https://nsidc.org/data/icesat-2/data, https://doi.org/10.1594/PANGAEA.894801, https://allencoralatlas.org/atlas/#12.42/-23.4644/151.9470

Keywords:
ICESat-2
Coral reefs
Machine learning
Rugosity
Heron island

ABSTRACT

As anthropogenic impacts threaten natural habitats, effective monitoring strategies are crucial. Coral reefs, among the most vulnerable ecosystems, traditionally employ monitoring techniques that are labor-intensive and costly, prompting the exploration of remote sensing as a cost-effective alternative. Launched in October 2018, the Ice, Cloud, and land Elevation Satellite-2 (ICESat-2) provides high-resolution, high-frequency data, with its green laser offering unprecedented opportunities for bathymetric and coral reef applications. This study investigates the use of ICESat-2 data for atoll coral reef detection, utilizing Heron Island in the Great Barrier Reef, AU, and employing machine learning models. A binary logistic regression (BLR) model and convolutional neural network (CNN) were tested for determining coral reef presence, with the CNN outperforming the BLR in accuracy (85.4%), F1 score (43%), and false positive rate (13.1%). A challenge of the study included the difficulty of balancing false positive rates in predictive models to avoid over- or underestimations of reef extent. These obstacles were mitigated through the integration of algorithmically derived pseudo-rugosity and slope metrics as innovative proxies for seafloor complexity, significantly improving predictive performance. Feature importance analysis identified satellite-derived bathymetry (SDB) depth as the most critical predictor of coral presence, followed by pseudo-rugosity, slope, and various other depth measurements. This research establishes a new application of ICESat-2 data combined with advanced machine learning techniques as a promising method for efficient and cost-effective coral reef monitoring. Future work should refine algorithms and incorporate additional environmental variables to improve model performance across various reef types.

1. Introduction

As anthropogenic impacts increasingly threaten natural and human habitats, it becomes imperative that relevant research is maintained to lessen these threats. Among the ecosystems susceptible to these changes, coral reefs and their associated benthic habitats stand out as particularly vulnerable. Current coral reef monitoring techniques, such as manta tow surveys and fixed site surveys using photography and visual counts, require significant human effort to collect *in situ* data (Australian Institute of Marine Science, 2023). Furthermore, these methods are restricted to small spatial extents, typically on the order of meters. These limitations highlight the need for scalable and cost-effective alternatives.

Remote sensing technologies provide a promising alternative solution for monitoring coral reefs across large spatial extents that is reliable, cost-effective, and economical. In geomorphic and habitat mapping, the literature identifies satellite imagery, such as multispectral imagery (Caras et al., 2017; Gazi et al., 2020; Li et al., 2020; Munawaroh et al., 2021), hyperspectral imagery (Mishra et al., 2007; Diaz et al., 2024), or a combination of both (Bajjouk et al., 2019) as the primary remote sensing datasets. Traditional light detection and ranging (LiDAR) instrumentation has also demonstrated exceptional capability in producing highly accurate and detailed coral reef maps (Harris et al., 2023; Amani et al., 2022). Satellite imagery offers large-scale coverage of the world, typically with frequent data acquisition, making it an effective data source for monitoring reef extent. However, satellite imagery is inherently limited by its inability to penetrate water and capture underwater features, a critical capability for detailed coral reef and bathymetric mapping. On the other hand, LiDAR data offers highly accurate, higher-resolution bathymetric data, making them ideal for assessing seafloor complexity. However, LiDAR systems are expensive, logistically challenging, and typically used for regional-scale mapping rather than broad, large-scale reef monitoring. Space-based LiDAR platforms such as the Ice, Cloud, and Land Elevation Satellite-2 (ICESat-2) represent an emerging alternative that combines the strengths of these two approaches. ICESat-2 provides wide-scale coverage similar to satellite imaging, while also delivering

* Corresponding author at: Center for Coastal and Ocean Mapping/UNH-NOAA Joint Hydrographic Center, University of New Hampshire, Durham, NH 03824, USA.
E-mail address: gabrielle.trudeau@unh.edu (G.A. Trudeau).

https://doi.org/10.1016/j.ecoinf.2025.103099
Received 19 December 2024; Received in revised form 3 February 2025; Accepted 7 March 2025
Available online 19 March 2025

bathymetric accuracy akin to LiDAR data, offering a balanced compromise between detail and accessibility. This unique capability makes ICESat-2 an advantageous tool for coral reef monitoring, enabling large-scale assessments with sufficient resolution to capture ecologically significant features.

ICESat-2 was launched in October 2018 to collect elevation measurements of the Earth. It follows as the second generation of the original laser altimeter, ICESat, that was in service from 2003 to 2009. While initially intended for collecting data regarding changes in the cryosphere, the green laser aboard ICESat-2 opens the door to an abundance of oceanic and bathymetric applications (National Snow and Ice Data Center, 2024). Initial studies have validated ICESat-2's capability for extracting bathymetry (Parrish et al., 2019; Ma et al., 2020; Ranndal et al., 2021). However, as a space-based LiDAR system, ICESat-2 faces challenges such as underwater light scattering and noisy photon signals, which can affect the quality and accuracy of its data for marine applications (Zhang et al., 2024; Xie et al., 2024; Song et al., 2024; Wen et al., 2024). Recent studies have introduced various filtering techniques (sometimes referred to as "denoising" or "decomposing") (Zhu et al., 2024; Yin et al., 2024; Wang et al., 2023) to address these challenges and improve the reliability of ICESat-2 data. Despite these challenges, extracting bathymetry using a single dataset such as ICESat-2 offers significant advantages, including simplicity, consistency, and reproducibility. It also streamlines workflows, such as our own, that rely on bathymetric data.

Many studies that evaluate ICESat-2's bathymetric performance in combination with other datasets, such as multispectral satellite imagery from Sentinel-2 (Babbel et al., 2021; Xu et al., 2021; Hsu et al., 2021; Gleason et al., 2021; Zhang et al., 2022), conclude that ICESat-2 alone does not provide a strong monitoring capability. Other notable approaches use deep learning with ICESat-2 and multispectral data for coral reef classification (Ai et al., 2024) and geomorphic zone mapping (Zhong et al., 2024). While combining datasets can enhance results, it also increases computational and analytical complexity and may introduce additional noise or errors, potentially impacting the reliability of the model and its outcomes.

Recent advancements in machine learning have seen a wide variety of models developed for predictive purposes (Abu-Hashem et al., 2024). Models such as the LSTM-INFO (Adnan et al., 2023) and RVM-DMOA (Adnan et al., 2024) have shown effectiveness in tasks such as time series modeling. These models often incorporate hybrid or ensemble approaches to enhance predictive accuracy and handle the temporal variations inherent in time series data. However, the task of coral reef detection presents unique challenges that differ from traditional time series applications. Although hybrid models can offer increased flexibility and predictive power, they often introduce additional complexity in model training and implementation, which may not be necessary for this application. We have opted to use models that efficiently capture spatial features while maintaining a straightforward architecture. This study achieves a balance between model performance and interpretability, ensuring that the methodology remains accessible while addressing the core challenges of the task.

To extend the utility of ICESat-2 data alone, numerical parameters such as slope and rugosity extracted from ICESat-2 are explored in this study. While these parameters have been explored in geomorphic studies, their application in comprehensive coral detection from LiDAR remains underutilized. Though studies on coral reef mapping naturally focus on sites with corals, there is a gap in the literature explicitly addressing the comprehensive detection of coral presence. This study addresses this gap by leveraging ICESat-2 data with machine learning techniques to detect coral reefs near Heron Island in the Great Barrier Reef, Australia. Using a binary logistic regression (BLR) model and convolutional neural network (CNN), this research evaluates the potential of ICESat-2 to be a cost-effective solution to coral reef detection and other related research. The results provide foundational insights into the utility of ICESat-2 data for marine applications and demonstrate its value as a reliable, high-resolution, and temporally frequent data source for monitoring coral reefs. By advancing remote sensing methodologies, this work contributes to the efficient processing and application of ICESat-2 data, with implications for both coral reef research and broader environmental monitoring efforts.

2. Materials and methods

2.1. Study area

Our study site is the coral cay of Heron Island (23° 27′ S., 151 ° 57′ E.) and a neighboring reef, Wistari Reef (23° 28′ S., 151° 53′ E.), located at the southern tip of the Great Barrier Reef in Australia (Fig. 1). These reefs are lagoonal reefs, also known as atolls, which are characterized by well-defined reef flats that slope downward along their perimeters and lagoons filled with coral patches. This unique and straightforward reef structure minimizes environmental complexity, making the site an ideal test bed for developing and validating a coral reef monitoring methodology. Additionally, these reefs, which are home to 72% of all coral species on the Great Barrier Reef, exhibit exceptionally high biodiversity. By selecting this site, we establish a strong foundation for testing and validating our approach under ideal conditions, maximizing the potential for accurate, reliable, and scalable monitoring of coral reefs. This proof of concept underscores the feasibility and effectiveness of our methodology, paving the way for its application in more complex and diverse reef environments.

2.2. ICESat-2 data

ICESat-2, containing the Advanced Topographic Laser Altimeter System (ATLAS) photon-counting instrument, utilizes a green laser (532 nm) to collect Earth elevation data. At each overpass, this laser surveys with three pairs of beams spaced 3.3 km apart, where each pair contains a strong and a weak beam spaced 90 m apart, resulting in six beams in total. The strong and weak beams differ in transmit energies with an approximate ratio of 4:1. With a footprint width of approximately 6.6 km across track, ICESat-2 releases 10,000 pulses per second, ideally providing a ground-based measurement every 70 cm on the strong tracks and 280 cm on the weak tracks (National Snow and Ice Data Center, 2024).

As a non-traditional dataset, ICESat-2 presents unique challenges. Unlike conventional LiDAR systems, its photon-counting approach generates high levels of noise, requiring significant filtering to distinguish true seafloor returns from noise photons. Additionally, the narrow footprint and widely spaced tracks limit its spatial coverage, preventing ICESat-2 from achieving global coverage. To mitigate these limitations and strengthen the signal in our study, the strong and weak tracks within each beam pair were combined.

The spatial coverage of the study area, shown in Fig. 2, is approximately 20 km x 11 km in area, with temporal coverage from 2019 to 2022. Twenty-three distinct ICESat-2 tracks from eight different dates in total were used in the study. The processing steps undertaken to extract bathymetry from ICESat-2 tracks are further discussed, with an example of a processed track shown in Fig. 4.

This study uses ICESat-2's data product ATL03, Global Geolocated Photons (Neumann et al., 2023), which were retrieved from the National Snow and Ice Data Center (NSIDC). The NSIDC provides a user's guide, algorithm theoretical basis document, and data dictionary for ATL03 (Neumann et al., 2023). ATL03 uses lower-level products to geolocate returned photon events in X, Y, and Z directions and to classify their heights. These classifications include a photon quality flag and a photon signal confidence flag. The quality flag (*quality ph*) classifies data as nominal, possible after-pulse, possible impulse response, or possible transmitter echo pulse (TEP). The photon signal confidence flag (*signal conf ph*) classifies each photon based on the likelihood that it is a true signal (not noise) for different surface types (i.e., land, ocean, sea ice, land ice, and inland water). Each photon is assigned a confidence value indicating noise (0), background (1), low confidence (2), medium confidence (3), or high confidence (4) for each surface type (Neumann et al., 2023). While this flag helps reduce data volumes for higher-level ICESat-2 products, it also serves as a signal-confidence rating that we leveraged for noise filtering.

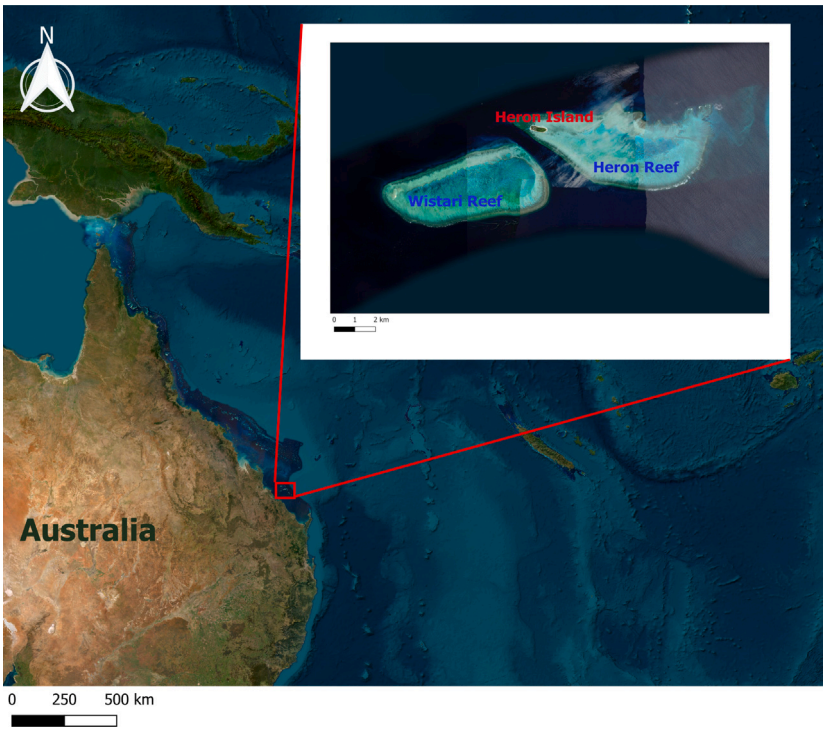

Fig. 1. Satellite image of Heron Island, AU and the surrounding reefs: Wistari and Heron Reef. Map lines delineate study area and do not necessarily depict accepted national boundaries.

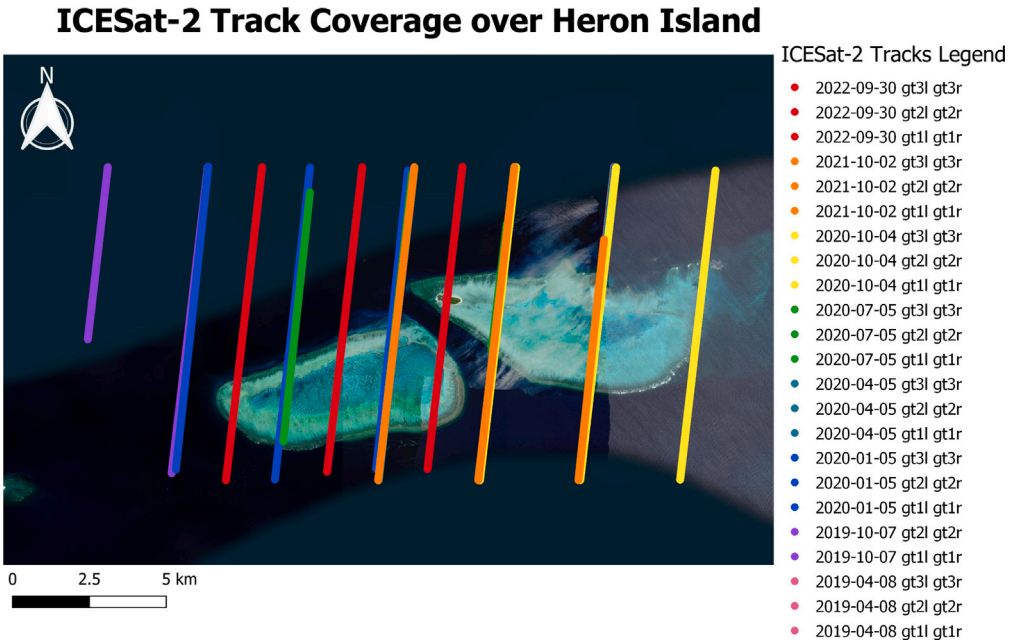

Fig. 2. All usable ICESat-2 tracks located within the study area. Each track is labeled with the date (year–month–day) the data were acquired and the specific subtracks it includes (ex. gt1l gt1r).

2.2.1. *Roselfsema photoquadrats*

Roelfsema et al. (2018) provides a dataset of underwater benthic photos taken in a 2017 photo-transect survey of the Great Barrier Reef, including Heron Reef. These photos are captured orthogonal to the seafloor, positioned 0.5 m above 1 m *x* 1 m photoquadrats placed along the benthos, while a GPS records the location of the center of each photo. This dataset will be further discussed for its use as ground-truth data in the validation of different geomorphic structures and algorithmically extracted rugosity values from ICESat-2 data.

2.2.2. *Allen Coral Atlas*

The Allen Coral Atlas (ACA) was created by Arizona State University as a coral conservation tool, using high-resolution imagery from Planet's PlanetScope satellites to map coral reefs around the world (Lyons et al., 2022). Combining remote sensing data, *in situ* data, and existing coral classifications, the ACA developed reef cover (geomorphic zones) and benthic cover classes. These classifications rely on physical attributes of the data, such as depth, slope, exposure, color, texture, and spatial relationships (Kennedy et al., 2021). This

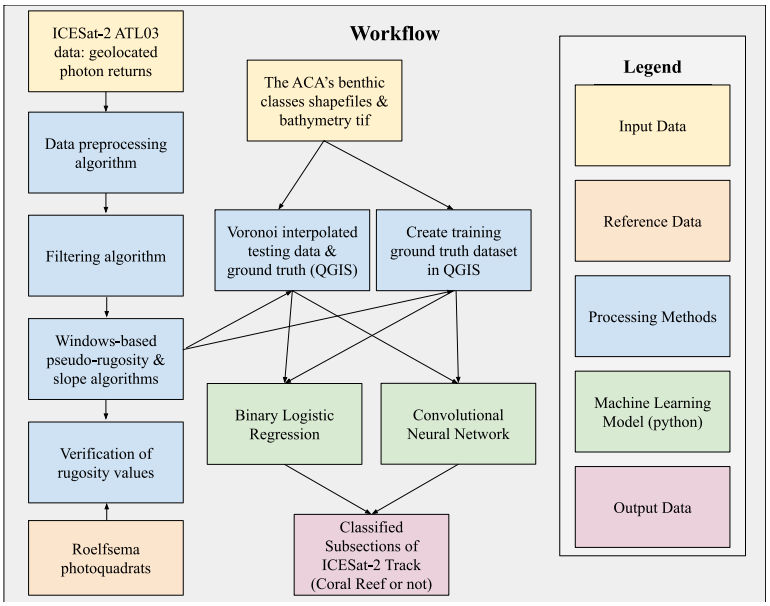

Fig. 3. Project workflow for data processing and data preparations for analysis.

dataset will be further discussed for its use in creating a ground-truth dataset. Also available from the ACA are satellite-derived bathymetry (SDB) values, derived from a composite spectral image created with Sentinel-2, Landsat-8, and Planet Dove images (Lyons et al., 2022).

2.3. Methodology

2.3.1. Workflow

The workflow for data processing and methods is found in Fig. 3; a more detailed description follows. The inputs to this workflow are ICESat-2's ATL03 geolocated photon returns for the tracks shown in Fig. 2, and the ACA's benthic classes shapefiles and SDB/depth geotif file. Additionally, the Roselfsema et al. photoquadrats (Roelfsema et al., 2018) are used as reference data. Two different modeling methods (binary logistic regression and convolutional neural network) were used to classify sections of ICESat-2 tracks as 'coral' or 'not coral'. In this context, 'coral' indicates that the window contains coral reef features. The following sections will elaborate on each stage of the workflow.

2.3.2. Data preprocessing and filtering

The data preprocessing algorithm combines the strong and weak ICESat-2 tracks, applies a refraction correction (Parrish et al., 2019), converts longitude and latitude coordinates to UTM Easting and Northing (X and Y) coordinates, converts ellipsoidal depths to orthometric depths, and converts the data into easily processable csv files. These steps were taken to deal with the sub-surface nature of coral reefs and the noise inherent in ICESat-2 data.

Next, the data were run through a series of steps that algorithmically identifies bathymetric photon events. Initially, a histogram was created for the distribution of depth values for each ICESat-2 track. ICESat-2 tracks are considered to be a straight line; thus, we utilized the UTM Northing coordinate to represent the along-track direction and assumed the UTM Easting coordinate does not differ substantially. The number of histogram bins was set to one-fourth of the number of photon events in the current track. The depth of the ocean surface was identified by selecting the depth (histogram bin) with the highest density of points. All points along the ocean surface or above were removed. Concurrently, the laser's extinction point – i.e., the depth of the ocean beyond which LiDAR will not penetrate – was determined by analyzing the deepest reliable depth recorded from data categorized as a signal with high or medium confidence and nominal quality.

Following the removal of surface and excessively deep points, any remaining noise was filtered out using confidence and quality flags from ICESat-2. Photons classified as nominal by the quality flag (most likely to not be noise) and that had a medium or high confidence flag for any surface type (i.e., ocean, sea ice, etc.) were retained as bathymetry. Post-filtering, any retained bathymetric points were considered to be the surface of the seafloor. Additionally, tracks containing fewer than 20 bathymetric points along the entire track post-filtering were excluded from further analysis (See Fig. 4 for an example of the results of these filtering procedures).

2.3.3. Pseudo-rugosity and slope: Parameter extraction from ICESat-2 data

2.3.3.1. Pseudo-rugosity.

Following the creation of files containing algorithmically extracted seafloor points, the focus shifted to extracting additional seafloor features that may indicate the presence/absence of coral reef. It is well accepted in the benthic ecology community that rugosity serves as a proxy for the presence and frequency of coral reefs (i.e., low rugosity typically indicates fewer scleractinian corals, while high rugosity suggests a greater abundance) and the presence of coral reefs. Similarly, slope has been widely recognized as a key indicator for identifying geomorphic zones (as defined by the ACA), as it reflects the structural characteristics of the reef. In this study, we extracted a measure of slope and rugosity, which we refer to as "pseudo-rugosity", from the points denoting the surface of the seafloor. Our windows-based "pseudo-rugosity" algorithm is inspired by the "chain-and-tape" method commonly used *in situ* to describe the complexity of a coral reef surface. The method calculates a ratio (R) based on the length of a chain draped over the seafloor profile (L) compared to the distance covered when the chain is fully extended (D) (Walbridge et al., 2018) (Fig. 5) :

$$R = \frac{L}{D} \tag{1}$$

First, each ICESat-2 track was segmented into non-overlapping 20 m windows (i.e., subsections); unless otherwise stated, the term "window" is adopted throughout. To reduce any possible remaining noise from the data, each window was further segmented into 0.5 m sub-windows, for which the minimum and median depth (Z, in meters) values were calculated. The median depth was likely to provide a more representative measure of the depth within each 0.5 m sub-window, while the minimum depth values were least likely to be noisy. During

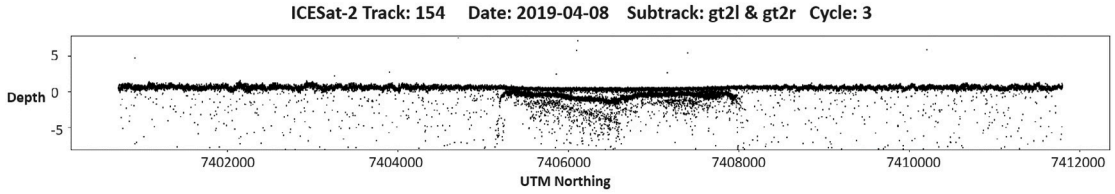

(a) Unfiltered ICESat-2 track.

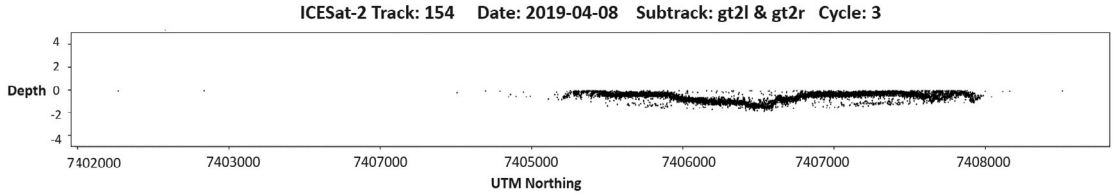

(b) Filtered ICESat-2 track, with seafloor extracted.

Fig. 4. Example of an ICESat-2 track pre and post filtering. (a) depicts an unfiltered track. (b) depicts a filtered track where a best algorithmic estimate of the seafloor remains.

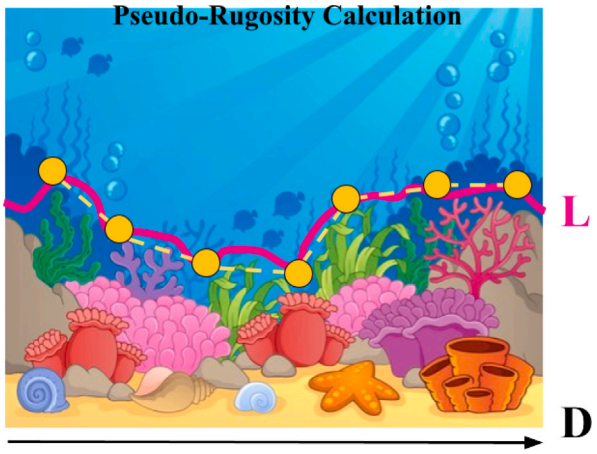

Fig. 5. A graphic of the windows-based pseudo-rugosity algorithm based on the "chain-and-tape" method used to collect *in situ* data. Imagining the yellow dots represent ICESat-2 points, L is constructed using the distance between each neighboring point. D is calculated by taking the length of the window. Rugosity is equal to the ratio of L to D. (For interpretation of the references to color in this figure legend, the reader is referred to the web version of this article.)

the development of this methodology, the significance of each value in coral reef detection was uncertain, so both were retained. The median depth was used for subsequent pseudo-rugosity calculations. This approach reduced redundancy in geographically overlapping data points and minimized overall data volume, possibly resulting from combining strong and weak tracks. A pseudo-rugosity value was calculated for each 20 m window, and the leading edge of each 20 m window was saved as the location of that window. The distance $\hat{L}$ between two adjacent ICESat-2 points within a 20 m window ($\hat{L}$) was calculated using the Euclidean distance formula (Weisstein, 2024a):

$$\hat{L} = \sqrt{(y_2 - y_1)^2 + (z_2 - z_1)^2} \tag{2}$$

where Y is the UTM Northing coordinate and Z is the depth value. L is the sum of all $\hat{L}$ within the window. For a window containing N points, there are $N-1$ estimated chain lengths, denoted as $\hat{L}$. L is then divided by 20 m (D; the length of the window), which then produces a rugosity value for that window. We assumed minimal deviation in the UTM Easting direction, as ICESat-2 tracks are considered to be a straight line.

Given the nature of ICESat-2 data, where not every 20 m window of each track contained bathymetric points, the pseudo-rugosity algorithm considered multiple scenarios to ensure comprehensive data were captured across window boundaries. If a window contained no bathymetric points, it was assigned an error value of 999 and omitted from further analysis. If a window contained only one point, a rugosity value was not calculated, but that point does contribute to the rugosity calculation of adjacent windows. Windows with two or more points had their rugosity value partially constructed from points within the window, and additional values were computed using adjacent windows. Special cases were considered for windows at the beginning, end, or middle of a track, and detailed procedures for handling these scenarios are described in Appendix A.

The rationale behind assigning error values and omitting windows without bathymetric points was to maintain the integrity of the analysis by filtering out noise or incomplete data. Given that ICESat-2 data can be sparse in certain regions due to environmental or instrumental factors, a method was necessary to ensure that the points contributing to the rugosity calculation accurately reflected the underlying seafloor. The decision to incorporate points from adjacent windows for the calculation in windows with two or more points helps to capture the local variability on the seafloor, ensuring that all available data are utilized effectively. This approach minimizes the impact of sparse or incomplete information, while also utilizing as much of the data as possible, leading to more accurate and comprehensive analysis.

2.3.3.2. Slope.

Slope was extracted from ICESat-2 data using the parameter extraction algorithm. The goal of this slope measurement was not to produce a "true" slope value, but instead to measure something we anticipate is indicative of reef presence. The slope algorithm employed followed the same 20 m window and scenario-based structure as the pseudo-rugosity algorithm. Slope was calculated between each neighboring ICESat-2 point within a window using the formula (Weisstein, 2024b) (Fig. 6):

$$s = \frac{z_2 - z_1}{y_2 - y_1} \tag{3}$$

where Y is the UTM Northing coordinate and Z is the depth value. The slope equation used is well-suited for ICESat-2 data because it operates on point-based measurements of elevation and spatial coordinates, aligning with the satellite's along-track sampling structure and ensuring accurate steepness estimation over small spatial scales.

The resulting slope value per window was the average of the absolute value of all slopes calculated within that window. We assigned an error value of 999 to any window with 0 or 1 point and removed

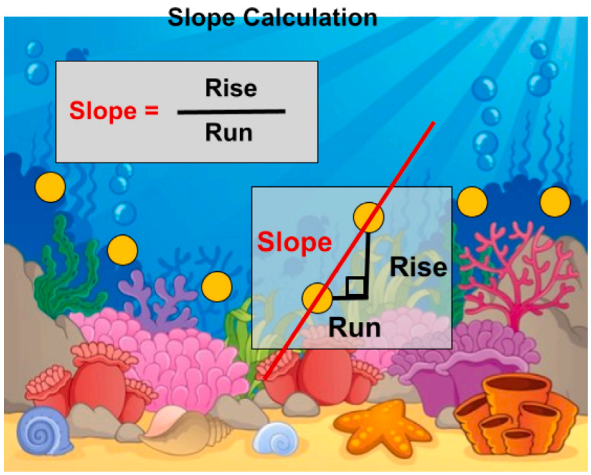

Fig. 6. A graphic of the slope calculation. Imagining the yellow dots represent ICESat-2 points, the slope between two points is calculated by dividing the change in elevation (the rise) over the change in distance (the run). (For interpretation of the references to color in this figure legend, the reader is referred to the web version of this article.)

these windows from our dataset. Additionally, slope values of higher than 300% were discarded as erroneous. The output of the parameter extraction algorithm was a data file containing coordinates, rugosity, slope and averaged depth values for each 20 m window of each ICESat-2 track, and were used as inputs to the machine learning models. We note that the 20 m window data structure created in these algorithms will be maintained moving forward.

2.3.4. Ground-truth dataset

A ground-truth dataset is essential for the verification of any machine learning algorithm. Our model aims to classify each distinct 20 m ICESat-2 window as containing coral reef or not. This was facilitated by utilizing QGIS (a free and open source GIS software (QGIS Development Team, 2024)) that allows for easy manipulation and visualization of remote sensing data.

The QGIS workflow began by loading the processed ICESat-2 data, as well as the ACA's benthic classes shapefiles and bathymetry geotif file. The goal was to construct a ground-truth dataset that mirrors the spatial structure of ICESat-2 tracks while integrating the ACA's benthic class information. The dataset produced by this workflow was then used for model fitting, where each row represents an individual 20 m window, labeled with the predicted variable ('coral' or 'not coral') and containing predictor variables, such as rugosity, depth, etc. The output of the parameter extraction algorithm was individual csv files for each ICESat-2 track reduced to 20 m windows, containing coordinates, SDB, depth, and extracted parameters of rugosity and slope. The files produced were first converted into vector shapefile formats and separate tracks were then combined into a single file. The ACA's benthic classes for coral/algae and rock were combined to produce a single shapefile representing 'coral' and 'not reef.' This merged class taxonomy (Fig. 7) aligns with traditional ACA reef zones (crest, slope, and flats) and is likely to be detectable in ICESat-2 data.

To validate the decision to combine ACA classes, we performed a qualitative examination using photoquadrat data collected by Roelfsema et al. (2018). As shown in Fig. 7, areas classified as coral/algae and rock by the ACA coincided spatially with photoquadrats containing coral reef. Therefore, we proceeded to use the combined ACA's rock and coral shapefiles as ground-truth for our reef classification.

Next, we merged ICESat-2 data with the reef shapefile to generate a csv file. This csv file contains labels '1' (reef) and '0' (not reef) for each ICESat-2 window, which were based on spatial overlap with the reef shapefile. Furthermore, SDB data from the ACA were extracted for the center of each window. The resulting csv, visualized in Fig. 8, serves as the foundational dataset for training the machine learning models.

2.3.5. Surface generation from ICESat-2 data for testing

The ICESat-2 tracks for Heron and Wistari reefs do not provide complete coverage for the entire area (Fig. 2). Though the traditional approach for building machine learning models would be to split the ICESat-2 tracks and their associated 'coral'/'not coral' classes into testing and training sets, this method does not provide any insight into the model's performance across the entire study site. To validate the model over the entire study site, including areas not covered by ICESat-2 tracks, we used Voronoi polygons (also known as Thiessen polygons). These polygons were constructed using the center points of each 20 m window to estimate input parameters derived from ICESat-2 data, such as depth, slope, and rugosity. These polygons define areas of influence around each sample point, ensuring all points within a polygon are closer to its corresponding sample point than to any other (Yamada, 2016). Fig. 9 illustrates a graphical representation of Voronoi polygon construction across the entire study area.

By dividing the study area into Voronoi polygons using ICESat-2 data as sample points, we assigned specific attribute values, including rugosity, slope, and minimum and median depth to each polygon. Coordinates for the center of each polygon (UTM Easting and Northing) and SDB were obtained using QGIS and the ACA's SDB bathymetry file. Ground-truth labels of 'coral' or 'not coral' for this dataset were obtained utilizing the ACA's benthic class shapefiles. The resulting surface, composed of Voronoi polygons labeled as 'coral' or 'not coral', was used for testing the machine learning models. This process did not produce a smooth surface; instead, each polygon represents a window with a single value, reflecting the discrete nature of the data and the lack of spatial auto-correlation in coral locations throughout the lagoon.

2.3.6. Machine learning models

To achieve the best possible accuracy in identifying coral reefs along ICESat-2 tracks, we employed two different modeling methodologies: binary logistic regression (BLR) and convolutional neural network (CNN), both implemented in Python. The BLR serves to model general trends and relationships within the data, offering a straightforward and interpretable baseline for understanding the broader patterns of coral reef presence. In contrast, the CNN algorithm is designed to exploit finer details or "micro trends" in the dataset, which may lead to improved classification performance. A simple CNN architecture was selected over hybrid or more complex models due to its balance of performance, computational efficiency, and interpretability. This simplicity ensures the model is efficient and robust while avoiding unnecessary overhead, making it particularly well-suited for this application.

The variables used to train and test both models were rugosity, slope, the UTM Easting (X) and Northing (Y) coordinates of the initial edge of each window, the minimum and median depth values of ICESat-2 photon events algorithmically identified as bathymetry for a given window, and the ACA's SDB. Analysis indicated that all variables were statistically significant with a p-value of less than 0.0001. Both models were trained on all available windows for ICESat-2 tracks, while testing was conducted on labeled parameters extracted from the generated Voronoi polygon surface.

Due to the positioning of ICESat-2 tracks over this reef, there exists an inherent imbalance in the training data, with approximately 1 track containing coral for every 9 tracks that do not. This imbalance posed a risk of the models disproportionately favoring the majority class ('not coral') during training. To address this imbalance and minimize potential overfitting, several precautionary steps were implemented for both models. First, models were fit with balanced class weights to adjust for the disproportionate representation of classes in the data. Balancing the data adjusts the weights for each class based on the frequencies of each class in the data. For example, the weights for class 1 are calculated as:

$$w = \frac{N}{(n \cdot c)} \tag{4}$$

Fig. 7. Visualization of the ACA's benthic classes with Roelfsema et al.'s photoquadrat images (Roelfsema et al., 2018). The blue indicates the coral/algae benthic class, while the green indicates the rock benthic class. (For interpretation of the references to color in this figure legend, the reader is referred to the web version of this article.)

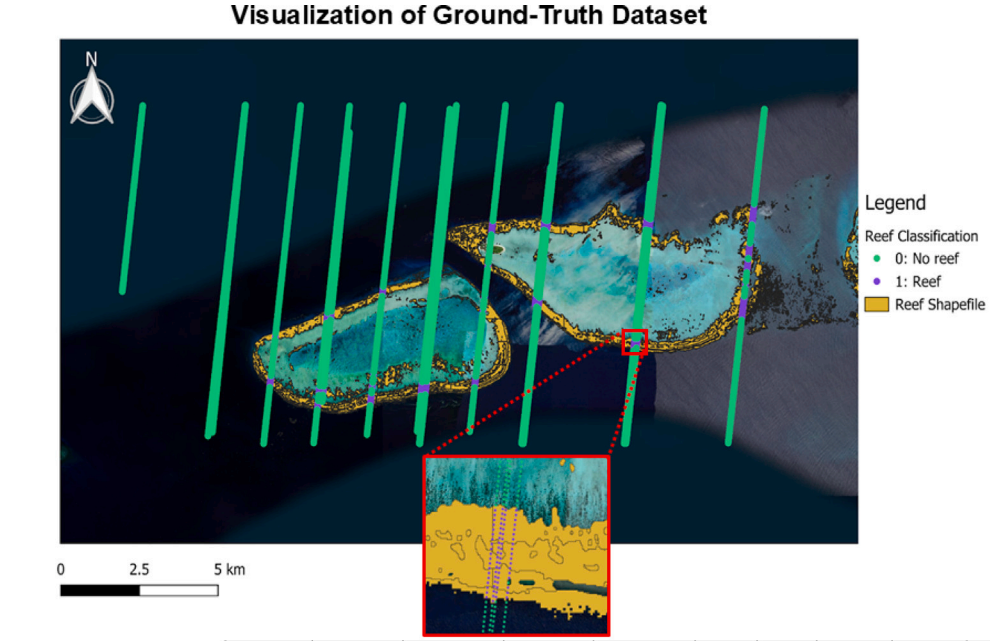

Associated csv File

Rugosity	Window Left X	Window Left Y	Window Right X	Window Right Y	Reef?	Bathy	Min Z	Med Z	Slope
1.002	383676.64	7402040.86	383678.46	7402060.86	1	6	-0.9847	-0.7599	15.01
1.003	383738.31	7402040.86	383740.12	7402060.86	0	2	-0.8254	-0.4080	10.84
1.001	383740.12	7402040.86	383741.94	7402060.86	0	10	-0.4749	-0.3354	12.61

Fig. 8. Visualization of ground-truth dataset created in QGIS, where each point indicates a 20 m ICESat-2 window. The green dots indicate no reef presence and the purple dots indicate reef presence. An example of an associated csv file can be found at the bottom of the figure, where each row represents a point in the map. (For interpretation of the references to color in this figure legend, the reader is referred to the web version of this article.)

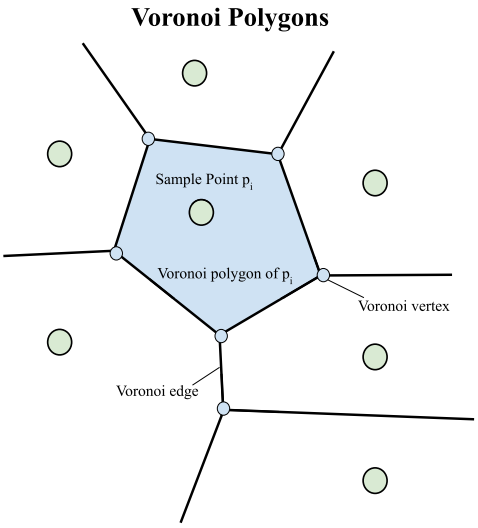

Fig. 9. Graphical depiction of Voronoi polygons, illustrating how each polygon is constructed around sample points, with boundaries equidistant between neighboring sample points.

where w is the weight assigned to class 1, N is the total number of samples, n is the number of classes, and c is the number of class 1 samples in the data (Pedregosa et al., 2023b). Second, all input variables were standardized, allowing us to compare data with different scales by scaling to unit variance. Standardized data were calculated as:

$$z = \frac{(x - \mu)}{\sigma} \tag{5}$$

where z is the standardized data, x is the sample value, μ is the mean of the data and σ is the standard deviation of the data (Pedregosa et al., 2023a). Finally, L2 (i.e., ridge regression) penalties were added to both models to mitigate overfitting. Together, these steps ensured that the models accounted for the imbalanced nature of the data and maintained robust performance across all classes.

Binary logistic regression (BLR) models classify data using the logistic sigmoid function, which constrains the output to a range between 0 and 1. The BLR employed here aims to classify ICESat-2 data by estimating the probability that a given window contains coral. This was done using the standard logistic regression model from *sklearn.learn_model*, with the *L-BFGS* solver. The *L-BFGS* solver is a quasi-Newton optimization method that uses a limited-memory version of the Broyden–Fletcher–Goldfarb–Shanno (BFGS) algorithm (Encyclopedia of Mathematics, 2024). L-BFGS is particularly well-suited for large-scale problems because it reduces memory usage by approximating the Hessian matrix using only a few vectors. The maximum number of iterations was set to 10000 to ensure convergence. Hyperparameters of the model, such as the solver method and tolerance, were fine-tuned using a grid search technique to enhance model performance and achieve the best classification results.

Convolutional neural networks (CNN) use a combination of convolutional layers, pooling layers, and dense layers in order to make predictions using data with a grid-like topology (Goodfellow et al., 2016). Initially, a CNN learns and extracts features through convolution and max pooling. The final classification was performed using fully connected layers. The CNN's structure was designed to identify patterns in the data that indicate the presence of coral reefs. For a detailed understanding of CNNs, refer to Goodfellow et al. (2016), Madhavan (2021).

After exploring alternatives, including 2-D convolutions with observation stacking, we found that a 1-D convolutional structure was most effective for analyzing the linear and time-series-like ICESat-2 data. This architecture aligns with the sequential nature of ICESat-2 tracks, where observations are ordered spatially along the satellite's path, making 1-D convolutions ideal for capturing local spatial patterns without unnecessary complexity. The CNN architecture, depicted in Fig. 10, contains two sets of convolutional and max pooling layers, followed by a flattening layer and a fully connected activation layer. The first layer of the model was a convolutional layer with 22 nodes, a (5×1) window, and ReLU activation. The second layer was a (2×1) max pooling layer. The third layer was another convolutional layer with 44 nodes, a (3×1) window, and ReLU activation. The fourth layer was a (2×1) max pooling layer. The fifth layer was a flattening layer, which takes our data from $(7 \times 1 \times 44)$ to (308×1). The final layer was a dense layer with ReLU activation that produced a binary classification output.

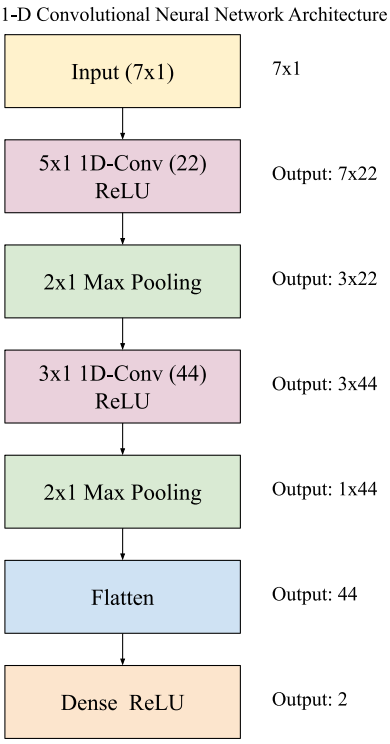

Fig. 10. Architecture of 1-D CNN.

The CNN was implemented using the sequential model from *tensorflow.keras* and utilizes the *adam* optimization solver, which combines the benefits of the stochastic gradient descent method with adaptive learning rates to improve convergence efficiency (Keras, 2023). To mitigate overfitting, early stopping with a patience of 50 epochs was employed to minimize loss and ensure that training stopped when the validation loss ceased improving. L2 regularization was strategically applied to the convolutional layer that exhibited greater influence within the model, helping to constrain the weights and reduce overfitting. Additionally, hyperparameters of the model, such as the learning rate, batch size, and number of nodes, were fine-tuned using a grid search technique to optimize performance and achieve the best results possible.

2.3.7. Feature importance analysis

Identifying the most important features in ML algorithms is crucial for understanding which variables influence the model's ability to detect coral reefs. For the BLR models, feature importance was defined by comparing the absolute value of the standardized scores for each variable. Standardized scores are calculated by subtracting the expected value according to the null hypothesis (typically zero) from the BLR regression coefficients, and then dividing by their associated standard errors. Neural networks are often described as "black boxes" because,

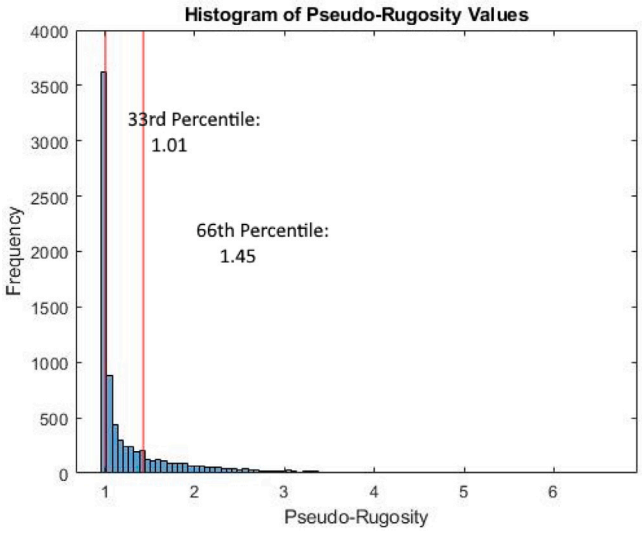

Fig. 11. Histogram of the distribution of pseudo-rugosity values. Values below the 33rd percentile are classified as low rugosity, values above the 66th percentile are classified as high rugosity, and values between the two thresholds are classified as medium rugosity.

although we know how they work, we are often unable to explain the patterns they extract from the data in order to make classifications. However, one way to determine the most important predictor variables is by measuring the permutation feature importance, which evaluates how the model's prediction error changes when each feature is permuted. For predictor error, we analyzed the changes in F1 score in relation to different combinations of features. Pseudo-code for this approach, provided by Molnar (Molnar, 2022), can be found in Appendix B.

3. Results

3.1. Parameter extraction results

The parameter extraction algorithm produced additional metrics from ICESat-2 data; namely, pseudo-rugosity and slope. These values provided insight into the variability of the seafloor's complexity across the study area. The following sections present the results of these metrics in both geographic and statistical contexts.

3.1.1. Pseudo-rugosity

Rugosity values were categorized into high, medium, and low groups for visualization, as shown in Fig. 11. Thresholds for these categories were determined using the 33rd and 66th percentiles of the rugosity distribution, identified through a histogram. Values below or equal to the 33rd percentile were classified as low, those between the 33rd and 66th percentiles as medium, and those above the 66th percentile as high. This approach ensures that the categories reflect the relative distribution of rugosity values, making it easier to compare and interpret them.

The results of the pseudo-rugosity algorithm displayed geographically are shown in Fig. 12.

Referencing 20 different photoquadrats from Roelfsema et al. (2018) that intersect with ICESat-2 tracks and are located along similar geomorphic structures, we were able to qualitatively verify that the pseudo-rugosity values are related to the geomorphology they describe. See Fig. 13 for examples of high, medium, and low rugosity classifications, the associated photoquadrat, and their location around Heron Reef. The photoquadrats associated with low rugosity were mostly sand, whereas those associated with high rugosity contained a variety of corals. Medium rugosity photoquadrats contained a mix of sand and corals or contained table/brush corals, such as *Acropora* spp.

3.1.2. Slope

Similarly to the pseudo-rugosity values, slope values were categorized into high, medium, and low groups for visualization. Fig. 14 shows the distribution of slope values. The thresholds for these categories were determined using the 33rd and 66th percentiles of the distribution, consistent with the approach used for rugosity.

The results of the slope algorithm displayed geographically are shown in Fig. 15.

Similar to the verification process for the pseudo-rugosity values, we used 20 different photoquadrats from Roelfsema et al. (2018) that intersect with ICESat-2 tracks to qualitatively verify that the slope values are related to the geomorphology they describe. See Fig. 16 for examples of high, medium, and low slope classifications, the associated photoquadrat, and their location around Heron Reef. The photoquadrats associated with low slope values were mostly flat sand areas or areas containing table/brush corals. In contrast, those associated with high slope values corresponded to steeper geomorphic features such as reef slopes. Medium slope photoquadrats contained mixtures of gently sloping coral structures, such as those located along the reef crest.

3.2. Model performance

The results of the machine learning models' 'coral'/'not coral' classification were summarized using metrics derived from the models' ability to predict 'coral,' including global accuracy, recall, F1 scores, false positive rate (FPR), and confusion matrices. Fig. 17 compares the performance of the BLR and CNN models in their ability to identify coral presence. The CNN demonstrated superior performance across multiple metrics. The BLR achieved a relatively high recall for coral predictions (92.9%), indicating effective identification of positive instances of coral reefs. However, this came at the cost of a high FPR for coral predictions (25.7%), meaning it frequently misclassified non-reef areas as coral. This tendency to overestimate coral presence introduces a bias in the BLR model, as seen in the F1 score (43%), potentially leading to an overestimation of coral reef coverage. In contrast, the CNN outperformed the BLR in terms of accuracy (85.4%) and FPR (13.1%) and produced a comparable F1 score to the BLR (49%). This demonstrates a more balanced performance in accurately predicting coral presence, thereby reducing the likelihood of overestimating coral coverage.

In addition to evaluating the models' ability to predict coral presence, it is important to assess how well they identify 'not coral' areas. The F1 score was chosen to provide a comprehensive measure of model performance, as it balances recall and precision. Major data imbalances, where one class (such as 'not coral' in our case) significantly outweighs the other, can lead to misleading F1 scores, potentially obscuring the model's true performance across both classes. While efforts have been made to address data imbalances during model development, we evaluate the F1 scores from both perspectives to gain a more holistic understanding of the models' overall performance. The BLR model achieved an F1 score of 85% for 'not coral' predictions, indicating a balanced performance in identifying non-reef areas with reasonable precision and recall. In comparison, the CNN outperformed the BLR with a higher F1 score of 91.5%, demonstrating stronger overall accuracy in distinguishing 'not coral' regions. Notably, the CNN's F1 score for 'not coral' predictions (91.5%) was slightly higher than its F1 score for coral predictions (49%), suggesting that the model is slightly more effective at identifying 'not coral' areas than coral regions. These results highlight the CNN's superior capability in identifying non-coral areas, making it a more effective model for this aspect of classification. Consequently, the CNN is more reliable in distinguishing "true" coral reef areas from non-reef features, as well as vice-versa, making it a more robust and balanced model compared to the BLR for this classification task.

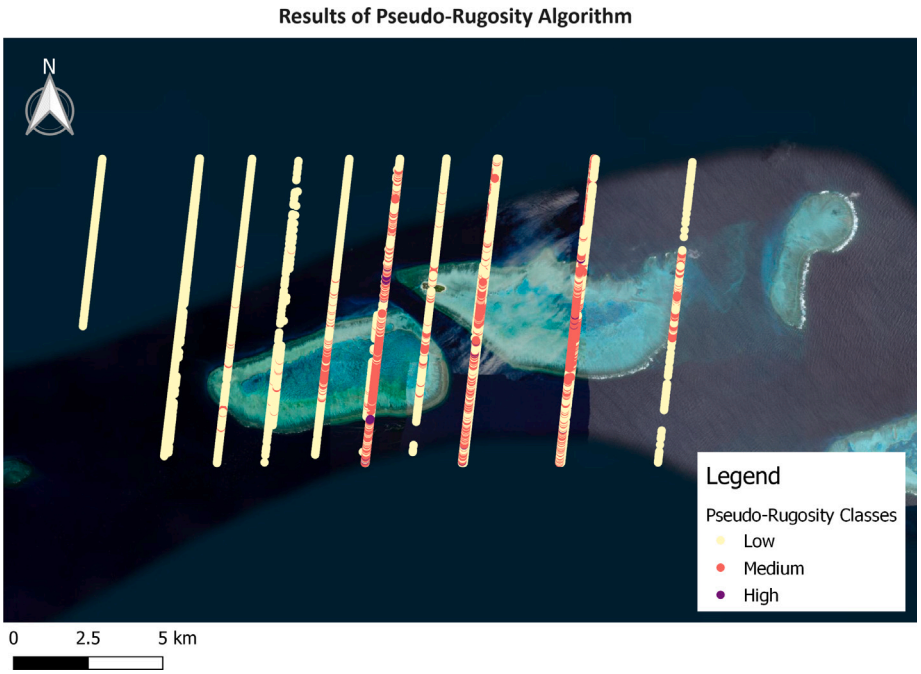

Fig. 12. Results of the pseudo-rugosity algorithm, categorized into high, medium, and low rugosity.

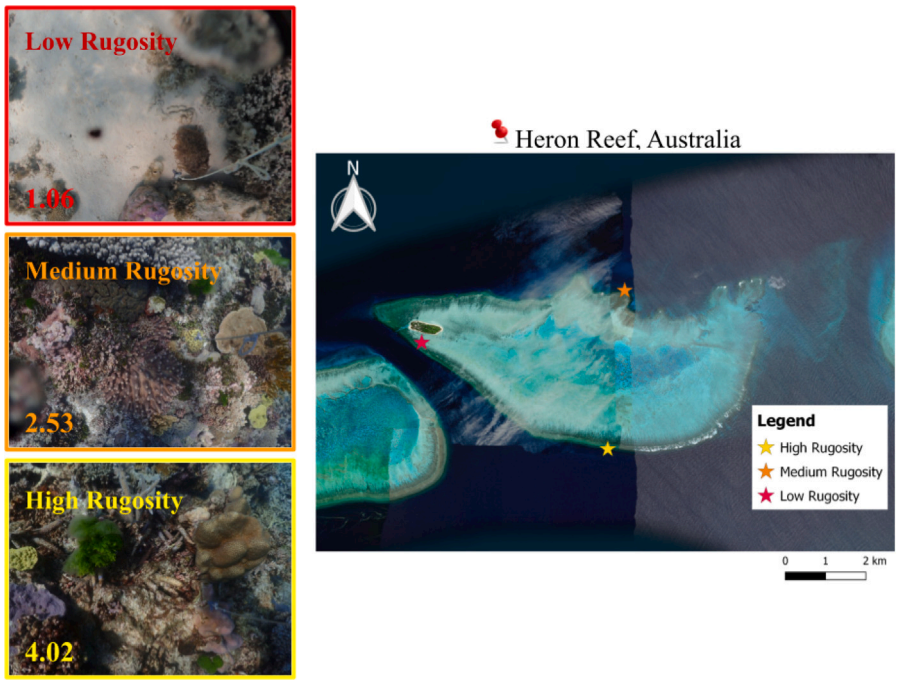

Fig. 13. Examples of high, medium, and low rugosity classifications, the associated photoquadrat and their location around Heron Reef. Photoquadrat images, part of a larger study conducted by Roelfsema et al. (2018) from 2011 to 2017, were collected in 2017. This study involved the collection of photoquadrats across the Great Barrier Reef.

3.3. Feature importance

Our feature importance analysis revealed that SDB was the most important feature in the BLR model, with rugosity and the UTM Easting coordinate as the next most important features (See Fig. 18). For the CNN, the associated features were ranked by changes in F1 score (See Fig. 19). Similarly to the BLR, SDB was identified as the predominant predictor. The minimum depth was the next most important, and rugosity and median depth were the next most important and roughly the same.

To assess how our algorithmically derived features (rugosity and slope) influence coral reef detection accuracy, we applied the permutation feature importance method to both the BLR and CNN models. Rather than focusing on which variable caused the greatest change in accuracy, we examined how much accuracy declined when each feature was excluded. Excluding rugosity reduced accuracy by 0.87% in the BLR and 0.01% in the CNN. Similarly, excluding slope resulted in a decrease of 0.2% in the BLR and 0.007% in the CNN. These results indicate that the BLR model is significantly more sensitive to changes in feature inclusion than the CNN. Furthermore, rugosity consistently had

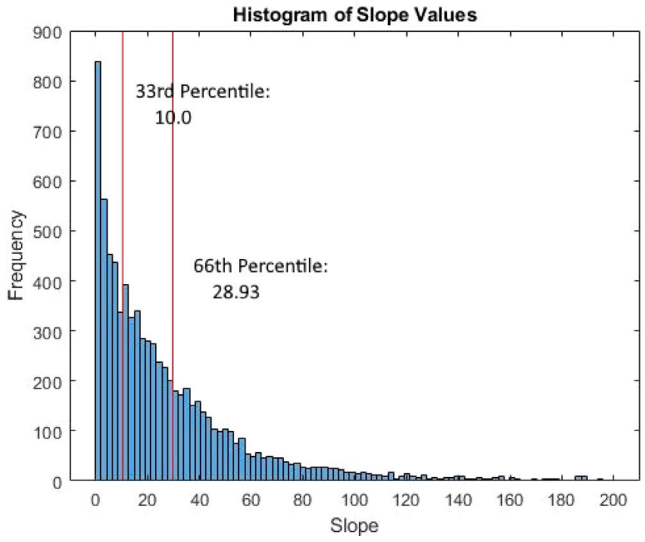

Fig. 14. Histogram of the distribution of slope values. Values below the 33rd percentile are classified as low slope, values above the 66th percentile are classified as high slope, and values between the two thresholds are classified as medium slope.

a greater influence on detection accuracy in both models, highlighting its critical role in identifying coral reefs.

4. Discussion

These steps toward identifying and delineating coral reef habitats establish a foundation for a reliable, cost-effective, and economical alternative for monitoring changes in coral reefs with a high-resolution and frequency dataset. In general, our results indicate that this method effectively identifies the presence of coral reefs. The application of convolutional neural networks (CNNs) offers promising results, suggesting satellite-based methods as a valuable tool for environmental monitoring. Furthermore, understanding the specific environmental variables driving coral reef detection enhances our ability to optimize and refine machine learning models, as well as direct decisions for data collection. Feature importance analyses identified SDB as the most important predictor in both models. If SDB is not readily available, a surrogate measurement may be needed. Rugosity, UTM coordinates, and depth variables also contributed substantially to the predictive capabilities of the models, underscoring their relevance in coral reef detection. While our rugosity and slope metrics were related to the geomorphology they describe, only rugosity proved to be an essential contributor to our models. The findings of this study suggest several practical implications for coral reef conservation and management, particularly in the context of remote sensing and machine learning.

The pseudo-rugosity and slope metrics developed in this study offer a proxy for coral reef presence. The use of ICESat-2 data, combined with the "chain-and-tape" inspired rugosity method and slope calculation, provided an innovative approach to remotely sensing benthic environments and effectively captured the complexity of the seafloor. Rugosity proved especially valuable for distinguishing coral reefs from smoother, non-reef areas, as indicated by its significant influence on model performance. Excluding rugosity caused noticeable declines in detection accuracy in both models, underscoring its critical role in coral reef detection. Similarly, slope contributed to detection accuracy, although its impact was less pronounced. These findings emphasize the importance of geomorphological features in refining coral reef detection models. Future research could integrate additional environmental variables and quantitative ground-truth data to improve model accuracy. Nonetheless, this study demonstrated the effectiveness of combining these metrics derived from ICESat-2 data for coral reef detection and established a foundation for its use in monitoring efforts.

The accuracy of our models' ability to identify coral reef presence directly impacts our estimation of coral reef extent, which is critical for ecological monitoring and conservation efforts. For instance, models with high recall but elevated FPRs, such as the BLR model, risk overestimating coral reef coverage. This misrepresentation can lead to inefficient resource allocation or misguided conservation efforts targeting non-reef areas. Conversely, false negatives, where actual coral reef areas are misclassified as non-coral, hinder conservation by leaving vulnerable reef areas unprotected. The CNN model, with its lower FPR and higher overall accuracy, reduces this bias by providing a more balanced approach that minimizes the risk of overestimation and offers a more accurate representation of coral extent. While this balanced approach reduces false positives and negatives, challenges remain in detecting subtle changes in reef extent, which is especially important for coral reef monitoring.

Despite the CNN's superior performance metrics and its potential for operational use in automated coral reef mapping from satellite data, limitations persist. These models may struggle to detect smaller or subtle changes in reef extent, particularly when applied to a monitoring methodology. These smaller changes may fall within the margin of error associated with the ICESat-2 data and the models, making it difficult to detect them reliably. Consequently, these methods are better suited for detecting substantial changes in reef coverage, which are more likely to be identified and confirmed with high certainty. Given that coral reefs typically change slowly under natural conditions, the models may only reliably detect larger changes occurring due to extreme weather events. Reducing both over- and under-estimations of coral coverage will improve the chances of detecting more subtle changes. However, this method's ability to detect large-scale changes is advantageous. For example, large-scale bleaching events result in the degradation of coral reefs and reduced rugosity, which can be identified by our model. This capability is advantageous for conservation and management, as it helps prioritize areas most susceptible to climate change impacts.

Through the use of ICESat-2 data, we illustrate the advantages of using satellite-based remote sensing for coral reef detection, addressing some of the limitations inherent in data traditionally used for coral reef research. ICESat-2 data are advantageous in this research because they are free to access and download, while traditional data collection methods are often costly and logistically challenging. The availability of ICESat-2's satellite data makes it a valuable resource for ocean-related research, allowing for wide-scale detection of coral reefs, especially for those reefs with limited access. Additionally, as more ICESat-2 data becomes available, we anticipate improved results. Specifically, an increase in data may make this method useful for detecting seasonal changes in coral reefs. This research contributes to the growing body of knowledge on the use of ICESat-2 data for ocean-related purposes and highlights the potential for further innovation in remote sensing techniques for environmental monitoring.

While the use of ICESat-2 data and CNN models presents numerous benefits, there are limitations that must be acknowledged. This study focused primarily on a specific geographic region and reef type; Heron Island and its atoll reefs. These reefs are characterized by well-defined reef flats, clear lagoonal waters, and relatively straightforward bathymetric features, which provide an optimal test bed for methodology development. Thus, it is important to note that the results of this study may not be perfectly transferable to non-lagoonal coral reefs. Reefs that lack the clear, abrupt transition from reef to non-reef may present challenges for the model. In these systems, the less defined boundary between the reef and non-reef areas could complicate the detection of features like rugosity. The model may experience reduced accuracy in such environments, where gradual transitions lead to less pronounced differences in physical characteristics. Additionally, variables critical to this model, such as SDB, may behave differently in ecosystems with

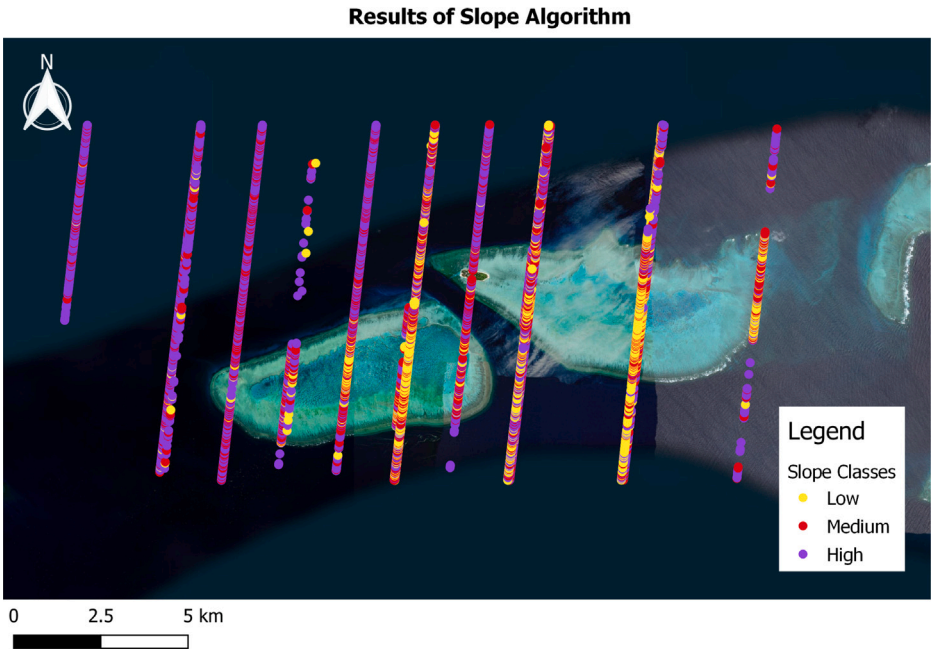

Fig. 15. Results of the slope algorithm, categorized into high, medium, and low slope values.

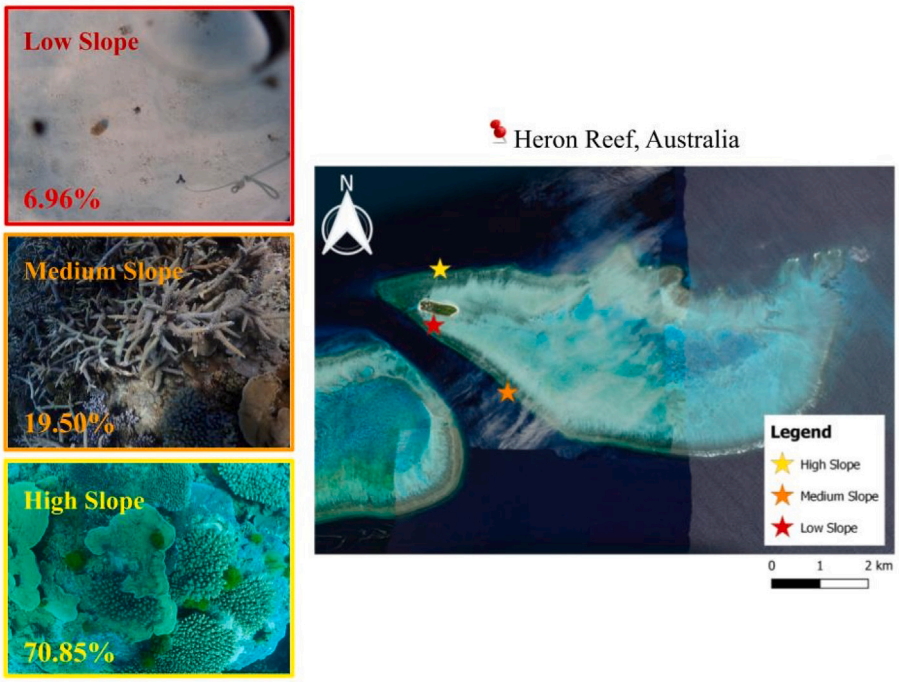

Fig. 16. Examples of high, medium, and low slope classifications, the associated photoquadrat and their location around Heron Reef. Photoquadrat images, part of a larger study conducted by Roelfsema et al. (2018) from 2011 to 2017, were collected in 2017. This study involved the collection of photoquadrats across the Great Barrier Reef.

unique physical and biological properties, requiring adjustments to the algorithm or the incorporation of new inputs. Despite these challenges, the methodology developed here lays a strong foundation for testing its scalability to other reef ecosystems and potentially broader marine environments. A natural next step in this research will be to extend the analysis to other diverse reef ecosystems to test the robustness and generalizability of our findings. Expanding the scope to include more varied reef types will provide insight into the limitations and adaptability of ICESat-2 data and machine learning models for global coral reef monitoring.

5. Conclusions

In conclusion, the integration of machine learning models with ICESat-2 remote sensing data offers a promising approach for advancing coral reef research and management. This study demonstrates the potential of combining seafloor complexity metrics, such as rugosity and slope, with machine learning to improve coral reef detection. Future research directions should prioritize continued exploration and refinement of machine learning algorithms, as well as the incorporation of additional environmental variables to enhance model accuracy. While the integration of rugosity and slope metrics provides key indicators

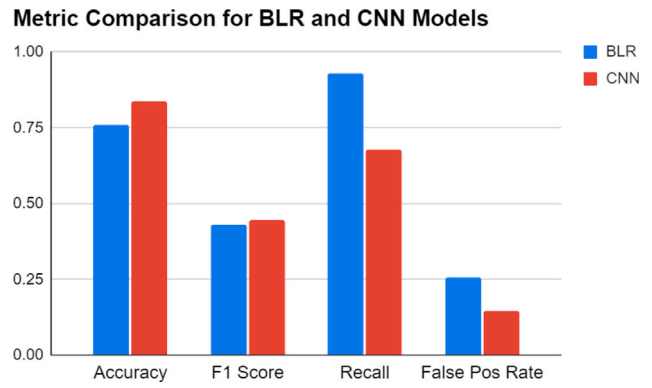

Fig. 17. Evaluative metrics for distinguishing 'coral' from 'not coral' for each machine learning model tested.

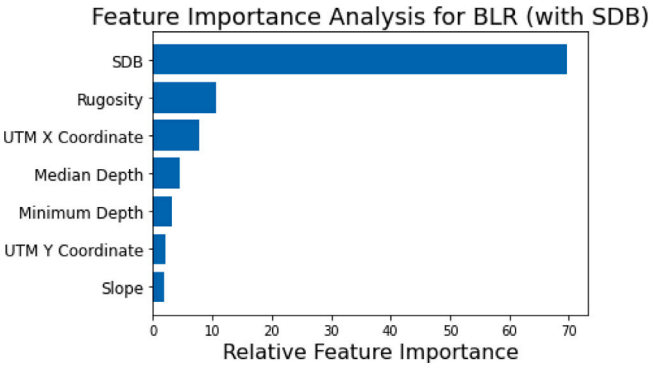

Fig. 18. Relative feature importance for the BLR model.

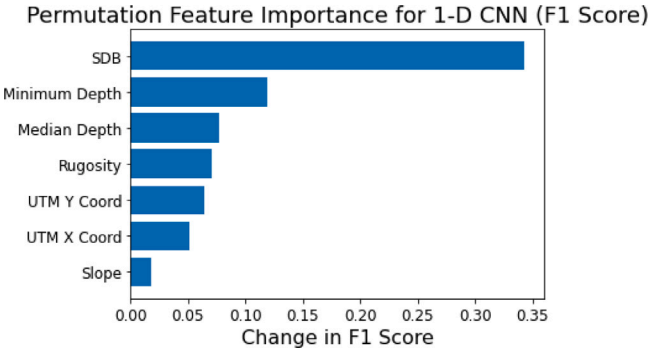

Fig. 19. Relative feature importance for the CNN using F1 score.

of seafloor complexity, these methods remain constrained by data availability and the challenges of validating results in remote coral reef environments. Addressing these challenges will require further *in situ* validation and an assessment of how well these approaches generalize across diverse reef ecosystems. The findings presented here not only advance the field of coral reef detection but also provide a foundation for future research aimed at utilizing ICESat-2 and similar datasets for broader environmental applications. By identifying areas of ecological importance and vulnerability, these methods empower policymakers and resource managers to allocate conservation efforts and funding more effectively. Furthermore, the ability to monitor reef conditions at large spatial scales supports adaptive management strategies, ensuring long-term assessment and response to environmental changes such as coral bleaching, coastal development, and climate-induced shifts in reef ecosystems. By harnessing advanced algorithms to enhance ecological research, particularly in spatial ecology, this study contributes to a more comprehensive understanding of coral reefs and supports their protection in the face of ongoing environmental challenges.

CRediT authorship contribution statement

Gabrielle A. Trudeau: Writing – review & editing, Writing – original draft, Visualization, Software, Methodology, Formal analysis, Conceptualization. **Kim Lowell:** Writing – review & editing, Supervision, Software, Methodology, Formal analysis, Conceptualization. **Jennifer A. Dijkstra:** Writing – review & editing, Validation, Supervision, Funding acquisition.

Declaration of Generative AI and AI-assisted technologies in the writing process

During the preparation of this work, the author(s) used ChatGPT and Grammarly to improve language, readability, and grammar. After using this tool/service, the author(s) reviewed and edited the content as needed and take(s) full responsibility for the content of the publication.

Declaration of competing interest

The authors declare that they have no known competing financial interests or personal relationships that could have appeared to influence the work reported in this paper.

Acknowledgments

This work was funded by the National Oceanic and Atmospheric Administration, United States under Grant number NA20NOS4000196.

Appendix A. Pseudo-rugosity algorithm pseudo code

We detail the specific scenarios for the two or more points case below:

If the current window is...

1. the first window of a track:
   (a) Calculate the distance between every point in the current window: $\hat{L}_{in}$.
   (b) Utilize the next window's first point to calculate the distance to the boundary of the window along the path from the current window's last point to the next window's first point: $\hat{L}_{next}$. If there are no points in the next window, $\hat{L}_{next}$ is calculated using the same depth as the current window's last point.
   (c) Sum all distances: $L = \sum \hat{L}_{in} + \hat{L}_{next}$

2. the last window of the track:
   (a) Calculate the distance between every point in the current window: $\hat{L}_{in}$.
   (b) Utilize the previous window's last point to calculate the distance to the boundary of the window along the path from the current window's first point to the previous window's last point: $\hat{L}_{prev}$. If there are no points in the previous window, $\hat{L}_{prev}$ is calculated using the same depth as the current window's first point.
   (c) Sum all distances: $L = \sum \hat{L}_{in} + \hat{L}_{prev}$

3. neither the first or last window of the track:
   (a) Calculate the distance between every point in the current window: $\hat{L}_{in}$.

(b) Utilize the previous window's last point to calculate the distance to the boundary of the window along the path from the current window's first point to the previous window's last point: $\hat{L}_{prev}$. If there are no points in the previous window, $\hat{L}_{prev}$ is calculated using the same depth as the current window's first point.

(c) Utilize the next window's first point to calculate the distance to the boundary of the window along the path from the current window's last point to the next window's first point: $\hat{L}_{next}$. If there are no points in the next window, $\hat{L}_{next}$ is calculated using the same depth as the current window's last point.

(d) Sum all distances: $L = \sum \hat{L}_{in} + \hat{L}_{prev} + \hat{L}_{next}$

L is then divided by 20 m (the length of the window) to derive the resulting pseudo-rugosity value for that window. Considering all possible scenarios ensures comprehensive data captured across window boundaries.

Appendix B. Permutation feature importance algorithm

Algorithm 1 Permutation Feature Importance Algorithm (Molnar, 2022)

Require: Trained model $\hat{f}$, feature matrix X, target vector y, error measure $L(y, \hat{f})$ (ie. accuracy, f1-score, etc.).

1: Estimate the original model error: $e_{orig} = L(y, \hat{f}(X))$
2: **for** each feature $j \in \{1, \ldots, p\}$, **do**
3: Generate feature matrix X_{perm} by permuting feature j in the data X.
4: Estimate error $e_{perm} = L(y, \hat{f}(X_{perm}))$ on predictions of the permuted data.
5: Calculate permutation feature importance as difference: $FI_j = e_{perm} - e_{orig}$
6: Sort feature by descending FI.

Data availability

ICESat-2 data is available for download from https://nsidc.org/data/icesat-2/data. The Roelfsema photoquadrats can be found at https://doi.org/10.1594/PANGAEA.894801 and were not modified. The shapefiles for the Allen Coral Atlas are available for download from https://allencoralatlas.org/atlas/#12.42/-23.4644/151.9470.

References

Abu-Hashem, Muhannad A., Shehab, Mohammad, Shambour, Mohd Khaled Yousef, Daoud, Mohammad Sh., Abualigah, Laith, 2024. Improved black widow optimization: An investigation into enhancing cloud task scheduling efficiency. Sustain. Comput.: Inf. Syst. (ISSN: 2210-5379) 41, 100949. http://dx.doi.org/10.1016/j.suscom.2023.100949, URL: https://www.sciencedirect.com/science/article/pii/S221053792300104X.

Adnan, Rana Muhammad, Mostafa, Reham R., Chen, Zhihuan, Parmar, Kulwinder Singh, Kisi, Ozgur, Zounemat-Kermani, Mohammad, 2023. Water temperature prediction using improved deep learning methods through reptile search algorithm and weighted mean of vectors optimizer. J. Mar. Sci. Eng. (ISSN: 2077-1312) 11 (2), http://dx.doi.org/10.3390/jmse11020259, URL: https://www.mdpi.com/2077-1312/11/2/259.

Adnan, Rana Muhammad, Mostafa, Reham, Dai, Hong-Liang, Mansouri, Ehsan, Kisi, Ozgur, Zounemat-Kermani, Mohammad, 2024. Comparison of improved relevance vector machines for streamflow predictions. J. Forecast. 43 (1), 159–181. http://dx.doi.org/10.1002/for.3028, arXiv:https://onlinelibrary.wiley.com/doi/pdf/10.1002/for.3028. URL: https://onlinelibrary.wiley.com/doi/abs/10.1002/for.3028.

Ai, Bo, Liu, Xue, Wen, Zhen, Wang, Lei, Ma, Huadong, Lv, Guannan, 2024. A novel coral reef classification method combining radiative transfer model with deep learning. IEEE J. Sel. Top. Appl. Earth Obs. Remote. Sens. 17, 13400–13412. http://dx.doi.org/10.1109/JSTARS.2024.3430899.

Amani, Meisam, Macdonald, Candace, Salehi, Abbas, Mahdavi, Sahel, Gullage, Mardi, 2022. Marine habitat mapping using bathymetric LiDAR data: A case study from bonne bay, newfoundland. Water (ISSN: 2073-4441) 14 (23), http://dx.doi.org/10.3390/w14233809, URL: https://www.mdpi.com/2073-4441/14/23/3809.

Australian Institute of Marine Science, 2023. Reef monitoring sampling methods. URL: https://www.aims.gov.au/research-topics/monitoring-and-discovery/monitoring-great-barrier-reef/reef-monitoring-sampling-methods.

Babbel, Benjamin J., Parrish, Christopher E., Magruder, Lori A., 2021. Icesat-2 elevation retrievals in support of satellite-derived bathymetry for global science applications. Geophys. Res. Lett. 48 (5), http://dx.doi.org/10.1029/2020GL090629, arXiv:https://agupubs.onlinelibrary.wiley.com/doi/pdf/10.1029/2020GL090629. URL: https://agupubs.onlinelibrary.wiley.com/doi/abs/10.1029/2020GL090629. e2020GL090629 2020GL090629.

Bajjouk, Touria, Mouquet, Pascal, Ropert, Michel, Quod, Jean-Pascal, Hoarau, Ludovic, Bigot, Lionel, Le Dantec, Nicolas, Delacourt, Christophe, Populus, Jacques, 2019. Detection of changes in shallow coral reefs status: Towards a spatial approach using hyperspectral and multispectral data. Ecol. Indic. (ISSN: 1470-160X) 96, 174–191. http://dx.doi.org/10.1016/j.ecolind.2018.08.052, URL: https://www.sciencedirect.com/science/article/pii/S1470160X1830654X.

Caras, Tamir, Hedley, John, Karnieli, Arnon, 2017. Implications of sensor design for coral reef detection: Upscaling ground hyperspectral imagery in spatial and spectral scales. Int. J. Appl. Earth Obs. Geoinf. (ISSN: 1569-8432) 63, 68–77. http://dx.doi.org/10.1016/j.jag.2017.07.009, URL: https://www.sciencedirect.com/science/article/pii/S0303243417301484.

Diaz, Gerardo, Lehahn, Yoav, Nantet, Emmanuel, 2024. Satellite-derived bathymetry in support of maritime archaeological research—VENUS imagery of caesarea maritima, Israel, as a case study. Remote. Sens. (ISSN: 2072-4292) 16 (7), http://dx.doi.org/10.3390/rs16071218, URL: https://www.mdpi.com/2072-4292/16/7/1218.

Encyclopedia of Mathematics, 2024. Broyden-Fletcher-Goldfarb-Shanno method. URL: http://encyclopediaofmath.org/index.php?title=Broyden-Fletcher-Goldfarb-Shanno_method&oldid=55449.

Gazi, Md, Mowsumi, Tahrim, Ahmed, Md. Kawser, 2020. Detection of coral reefs degradation using geospatial techniques around Saint Martin's Island, Bay of Bengal. Ocean. Sci. J. http://dx.doi.org/10.1007/s12601-020-0029-3.

Gleason, Arthur C.R., Smith, Ross, Purkis, Sam J., Goodrich, Kyle, Dempsey, Alexandra, Mantero, Alejandro, 2021. The prospect of global coral reef bathymetry by combining ice, cloud, and land elevation satellite-2 altimetry with multispectral satellite imagery. Front. Mar. Sci. (ISSN: 2296-7745) 8, http://dx.doi.org/10.3389/fmars.2021.694783, URL: https://www.frontiersin.org/articles/10.3389/fmars.2021.694783.

Goodfellow, Ian J., Bengio, Yoshua, Courville, Aaron, 2016. Deep Learning. MIT Press, Cambridge, MA, USA, http://www.deeplearningbook.org.

Harris, Daniel L., Webster, Jody M., Vila-Concejo, Ana, Duce, Stephanie, Leon, Javier X., Hacker, Jorg, 2023. Defining multi-scale surface roughness of a coral reef using a high-resolution LiDAR digital elevation model. Geomorphology (ISSN: 0169-555X) 439, 108852. http://dx.doi.org/10.1016/j.geomorph.2023.108852, URL: https://www.sciencedirect.com/science/article/pii/S0169555X23002726.

Hsu, Hsiao-Jou, Huang, Chih-Yuan, Jasinski, Michael, Li, Yao, Gao, Huilin, Yamanokuchi, Tsutomu, Wang, Cheng-Gi, Chang, Tse-Ming, Ren, Hsuan, Kuo, Chung-Yen, Tseng, Kuo-Hsin, 2021. A semi-empirical scheme for bathymetric mapping in shallow water by ICESat-2 and Sentinel-2: A case study in the South China Sea. ISPRS J. Photogramm. Remote Sens. (ISSN: 0924-2716) 178, 1–19. http://dx.doi.org/10.1016/j.isprsjprs.2021.05.012, URL: https://www.sciencedirect.com/science/article/pii/S0924271621001374.

Kennedy, Emma, Roelfsema, Chris, Lyons, Mitchell, Kovacs, Eva, Borrego Acevedo, Rodney, Roe, Meredith, Phinn, Stuart, Larsen, Kirk, Murray, Nicholas, Yuwono, Doddy, Wolff, Jeremy, Tudman, Paul, 2021. Reef cover, a coral reef classification for global habitat mapping from remote sensing. Sci. Data 8, 196. http://dx.doi.org/10.1038/s41597-021-00958-z.

Keras, 2023. Adam. URL: https://keras.io/api/optimizers/adam/.

Li, Jiwei, Fabina, Nicholas S., Knapp, David E., Asner, Gregory P., 2020. The sensitivity of multi-spectral satellite sensors to benthic habitat change. Remote. Sens. (ISSN: 2072-4292) 12 (3), http://dx.doi.org/10.3390/rs12030532, URL: https://www.mdpi.com/2072-4292/12/3/532.

Lyons, Mitchell, Larsen, Kirk, Skone, Matt, 2022. CoralMapping/AllenCoralAtlas: DOI for paper at v1.3. http://dx.doi.org/10.5281/zenodo.6622015, Zenodo.

Ma, Yue, Xu, Nan, Liu, Zhen, Yang, Bisheng, Yang, Fanlin, Wang, Xiao Hua, Li, Song, 2020. Satellite-derived bathymetry using the ICESat-2 lidar and Sentinel-2 imagery datasets. Remote Sens. Environ. (ISSN: 0034-4257) 250, 112047. http://dx.doi.org/10.1016/j.rse.2020.112047, URL: https://www.sciencedirect.com/science/article/pii/S003442572030417X.

Madhavan, Samaya, 2021. Introduction to convolutional neural networks. URL: https://developer.ibm.com/articles/introduction-to-convolutional-neural-networks/.

Mishra, Deepak R., Narumalani, Sunil, Rundquist, Donald, Lawson, Merlin, Perk, R., 2007. Enhancing the detection and classification of coral reef and associated benthic habitats: A hyperspectral remote sensing approach. J. Geophys. Res.: Ocean. 112 (C8), http://dx.doi.org/10.1029/2006JC003892, arXiv:https://agupubs.onlinelibrary.wiley.com/doi/pdf/10.1029/2006JC003892. URL: https://agupubs.onlinelibrary.wiley.com/doi/abs/10.1029/2006JC003892.

Molnar, Christoph, 2022. Interpretable Machine Learning, second ed. URL: https://christophm.github.io/interpretable-ml-book.

Munawaroh, Rudiastuti, AW, Dewi, RS, Ramadhani, YH, Rahadiati, A, Sutrisno, D, Ambarwulan, W, Pujawati, I, Suryanegara, E, Wijaya, SW, Hartini, S, 2021. Benthic habitat mapping using sentinel 2A: A preliminary study in image classification approach in an absence of training data. IOP Conf. Series: Earth Environ. Sci. 750 (1), 012029. http://dx.doi.org/10.1088/1755-1315/750/1/012029.

National Snow and Ice Data Center, 2024. ICESat-2. URL: https://nsidc.org/data/icesat-2.

Neumann, T.A., Brenner, A., Hancock, D., Robbins, J., Gibbons, A., Lee, J., Harbeck, K., Saba, J., Luthcke, S.B., Rebold, T., 2023. ATLAS/ICESat-2 L2A Global Geolocated Photon Data, Version 6. NASA National Snow and Ice Data Center Distributed Active Archive Center, http://dx.doi.org/10.5067/ATLAS/ATL03.006, URL: https://nsidc.org/data/ATL03/versions/6.

Parrish, Christopher E., Magruder, Lori A., Neuenschwander, Amy L., Forfinski-Sarkozi, Nicholas, Alonzo, Michael, Jasinski, Michael, 2019. Validation of ICESat-2 ATLAS bathymetry and analysis of ATLAS's bathymetric mapping performance. Remote. Sens. (ISSN: 2072-4292) 11 (14), http://dx.doi.org/10.3390/rs11141634, URL: https://www.mdpi.com/2072-4292/11/14/1634.

Pedregosa, Fabian, Varoquaux, Gaël, Gramfort, Alexandre, Michel, Vincent, Thirion, Bertrand, Grisel, Olivier, Blondel, Mathieu, Prettenhofer, Peter, Weiss, Ron, Dubourg, Vincent, Vanderplas, Jake, Passos, Alexandre, Cournapeau, David, Brucher, Matthieu, Perrot, Matthieu, Duchesnay, Édouard, 2023a. Sklearn.preprocessing.standardscaler. URL: https://scikit-learn.org/stable/modules/generated/sklearn.preprocessing.StandardScaler.html.

Pedregosa, Fabian, Varoquaux, Gaël, Gramfort, Alexandre, Michel, Vincent, Thirion, Bertrand, Grisel, Olivier, Blondel, Mathieu, Prettenhofer, Peter, Weiss, Ron, Dubourg, Vincent, Vanderplas, Jake, Passos, Alexandre, Cournapeau, David, Brucher, Matthieu, Perrot, Matthieu, Duchesnay, Édouard, 2023b. sklearn.utils.class_weight.compute_class_weight. URL: https://scikit-learn.org/stable/modules/generated/sklearn.utils.class_weight.compute_class_weight.html.

QGIS Development Team, 2024. QGIS geographic information system. Open Source Geospatial Foundation Project. https://www.qgis.org/.

Ranndal, Heidi, Sigaard Christiansen, Philip, Kliving, Pernille, Baltazar Andersen, Ole, Nielsen, Karina, 2021. Evaluation of a statistical approach for extracting shallow water bathymetry signals from ICESat-2 ATL03 photon data. Remote. Sens. (ISSN: 2072-4292) 13 (17), http://dx.doi.org/10.3390/rs13173548, URL: https://www.mdpi.com/2072-4292/13/17/3548.

Roelfsema, Christiaan M, Kovacs, Eva M, Stetner, Douglas, Phinn, Stuart R, 2018. Georeferenced Benthic Photoquadrats Captured Annually from 2002–2017, Distributed Over Heron Reef Flat and Slope Areas. Pangaea, http://dx.doi.org/10.1594/PANGAEA.894801.

Song, Yue, Ma, Yue, Zhou, Zhibiao, Yang, Jian, Li, Song, 2024. Signal photon extraction and classification for ICESat-2 photon-counting lidar in coastal areas. Remote. Sens. (ISSN: 2072-4292) 16 (7), http://dx.doi.org/10.3390/rs16071127, URL: https://www.mdpi.com/2072-4292/16/7/1127.

Walbridge, Shaun, Slocum, Noah, Pobuda, Marjean, Wright, Dawn, 2018. Unified geomorphological analysis workflows with benthic terrain modeler. Geosci. (Switzerland) 8, http://dx.doi.org/10.3390/geosciences8030094.

Wang, Bikang, Ma, Yi, Zhang, Jingyu, Zhang, Huanwei, Zhu, Haitian, Leng, Zihao, Zhang, Xuechun, Cui, Aijun, 2023. A noise removal algorithm based on adaptive elevation difference thresholding for ICESat-2 photon-counting data. Int. J. Appl. Earth Obs. Geoinf. (ISSN: 1569-8432) 117, 103207. http://dx.doi.org/10.1016/j.jag.2023.103207, URL: https://www.sciencedirect.com/science/article/pii/S1569843223000298.

Weisstein, Eric W., 2024a. Distance. URL: https://mathworld.wolfram.com/Distance.html.

Weisstein, Eric W., 2024b. Slope. URL: https://mathworld.wolfram.com/Slope.html.

Wen, Zhen, Tang, Xinming, Ai, Bo, Yang, Fanlin, Li, Guoyuan, Mo, Fan, Zhang, Xiao, Yao, Jiaqi, 2024. A new extraction and grading method for underwater topographic photons of photon-counting LiDAR with different observation conditions. Int. J. Digit. Earth 17 (1), 1–30. http://dx.doi.org/10.1080/17538947.2023.2295985.

Xie, Huan, Xu, Qi, Luan, Kuifeng, Sun, Yuan, Liu, Xiaoshuai, Guo, Yalei, Li, Binbin, Jin, Yanmin, Liu, Shijie, Tong, Xiaohua, 2024. Evaluating ICESat-2 seafloor photons by underwater light-beam propagation and noise modeling. IEEE Trans. Geosci. Remote Sens. 62, 1–18. http://dx.doi.org/10.1109/TGRS.2024.3363033.

Xu, Nan, Ma, Xin, Ma, Yue, Zhao, Pufan, Yang, Jian, Wang, Xiao Hua, 2021. Deriving highly accurate shallow water bathymetry from sentinel-2 and ICESat-2 datasets by a multitemporal stacking method. IEEE J. Sel. Top. Appl. Earth Obs. Remote. Sens. 14, 6677–6685. http://dx.doi.org/10.1109/JSTARS.2021.3090792.

Yamada, Ikuho, 2016. Thiessen polygons. In: International Encyclopedia of Geography. John Wiley & Sons, Ltd, ISBN: 9781118786352, pp. 1–6. http://dx.doi.org/10.1002/9781118786352.wbieg0157, arXiv:https://onlinelibrary.wiley.com/doi/pdf/10.1002/9781118786352.wbieg0157. URL: https://onlinelibrary.wiley.com/doi/abs/10.1002/9781118786352.wbieg0157.

Yin, Gaoying, Liu, Xin, Meng, Wenjun, Yang, Yang, Ding, Yurong, Li, Ruize, Guo, Jinyun, 2024. Adaptive OPTICS algorithm denoising icesat-2 laser photon data. IEEE Geosci. Remote. Sens. Lett. 21, 1–5. http://dx.doi.org/10.1109/LGRS.2024.3449446.

Zhang, Baichuan, Liu, Yanxiong, Dong, Zhipeng, Li, Jie, Chen, Yilan, Tang, Qiuhua, Huang, Guoan, Tao, Junlin, 2024. An optimal denoising method for spaceborne photon-counting LiDAR based on a multiscale quadtree. Remote. Sens. (ISSN: 2072-4292) 16 (13), http://dx.doi.org/10.3390/rs16132475, URL: https://www.mdpi.com/2072-4292/16/13/2475.

Zhang, Xuechun, Ma, Yi, Li, Zhongwei, Zhang, Jingyu, 2022. Satellite derived bathymetry based on ICESat-2 diffuse attenuation signal without prior information. Int. J. Appl. Earth Obs. Geoinf. (ISSN: 1569-8432) 113, 102993. http://dx.doi.org/10.1016/j.jag.2022.102993, URL: https://www.sciencedirect.com/science/article/pii/S1569843222001844.

Zhong, Jing, Sun, Jie, Lai, Zulong, 2024. ICESat-2 and multispectral images based coral reefs geomorphic zone mapping using a deep learning approach. IEEE J. Sel. Top. Appl. Earth Obs. Remote. Sens. 17, 6085–6098. http://dx.doi.org/10.1109/JSTARS.2024.3396374.

Zhu, Shuaiguang, Zhou, Guoqing, Yao, Ying, Li, Haowen, Han, Xiaoting, Li, Lin, 2024. A noise removal algorithm for photon counting LiDAR data: the ConvDS model. p. 92. http://dx.doi.org/10.1117/12.3052610.